Feshbach resonances, weakly bound molecular states, and coupled-channel potentials for cesium at high magnetic fields

Martin Berninger, Alessandro Zenesini, Bo Huang, Walter Harm, Hanns-Christoph Nägerl, Francesca Ferlaino, and Rudolf Grimm

Institut für Experimentalphysik and Zentrum für Quantenphysik, Universität Innsbruck, 6020 Innsbruck, Austria and Institut für Quantenoptik und Quanteninformation, Österreichische Akademie der Wissenschaften, 6020 Innsbruck, Austria

Paul S. Julienne

Joint Quantum Institute, NIST and the University of Maryland, 100 Bureau Drive Stop 8423, Gaithersburg, Maryland 20899-8423, USA

Jeremy M. Hutson

Joint Quantum Centre (JQC) Durham/Newcastle, Department of Chemistry, Durham University, South Road, Durham DH1 3LE, United Kingdom

(Received 21 December 2012; published 25 March 2013)

We explore the scattering properties of ultracold ground-state Cs atoms at magnetic fields between 450 G (45 mT) and 1000 G. We identify 17 previously unreported Feshbach resonances, including two very broad ones near 549 and 787 G. We measure the binding energies of several different dimer states by magnetic field modulation spectroscopy. We use least-squares fitting to these experimental results, together with previous measurements at lower field, to determine a six-parameter model of the long-range interaction potential, designated M2012. Coupled-channels calculations using M2012 provide an accurate mapping between the *s*-wave scattering length and the magnetic field over the entire range of fields considered. This mapping is crucial for experiments that rely on precise tuning of the scattering length, such as those on Efimov physics.

DOI: 10.1103/PhysRevA.87.032517 PACS number(s): 33.20.−t, 34.20.Cf, 34.50.Cx

I. INTRODUCTION

Cold cesium atoms have provided the foundation for many important experiments in basic science and also find application in precise atomic clocks. A thorough understanding of the collisions and interactions of two Cs atoms is crucial to interpret such experiments and optimize the applications. In particular, Cs has a complicated spectrum of magnetically tunable Feshbach resonances [1], which allow precise control of the two-body interactions. These resonances are due to near-threshold bound states of the diatomic molecule Cs_2 that can be tuned to match the near-zero energy of the colliding atoms. The resonances also allow an atomic sample to be converted with high efficiency into diatomic molecules by tuning an applied magnetic field across a resonance [2]. We have previously shown that the weakly bound molecules formed in this way can be converted into deeply bound [3] or even ground-state [4] molecules by stimulated Raman adiabatic passage.

Early work with Cs atoms and its interactions was at low magnetic field, $B \lesssim 250$ G [5]. Results on low-field Feshbach resonances [6–9] made it possible to construct theoretical models of the near-threshold bound and scattering states of two cold Cs atoms [9,10]. These models used the full Hamiltonian of Cs_2, including the potential energy curves of the $^1\Sigma_g^+$ singlet and $^3\Sigma_u^+$ triplet states, the molecular spin-spin interaction, and the atomic hyperfine interactions. Fitting the data allowed four key parameters of the model to be adjusted so that the resonance structure could be reproduced accurately in the low-field region. These early models yielded an understanding of the large clock shifts in Cs atomic fountain clocks [11], the anomalously large loss rates for collisions of doubly spin-polarized Cs atoms [12], and the magnetic field regions of moderate positive scattering length where Bose-Einstein condensation (BEC) was possible [13]. Subsequent measurements of the binding energies of weakly bound dimer states at fields up to 60 G [14,15] were mostly in good agreement with calculations based on the model of Ref. [9], which we designate M2004.

Ultracold Cs is particularly important for the study of Efimov states [16], which are high-lying bound states of triatomic molecules that appear when the two-body interaction has a bound state very close to threshold. Efimov states cause additional loss features close to two-body Feshbach resonances. The first observation of an Efimov resonance in Cs [17] was at a field near 8 G. We have recently extended this to observe Efimov features associated with three additional two-body Feshbach resonances, at fields up to 900 G, and reached the remarkable conclusion that the Efimov features all occur at almost the same two-body scattering length a and thus all have almost the same binding energy at unitarity ($a = \infty$) [18]. This universality of Efimov states was quite unexpected and contradicted previous theoretical indications [19], although subsequent theoretical work is now starting to explain its origins [20–23]. Efimov states in other ultracold systems are now also being found to show the same universal behavior [24–28].

The new Efimov resonances used to demonstrate universality in Ref. [18] are in the vicinity of two open-channel-dominated *s*-wave Feshbach resonances that were theoretically predicted with pole positions around 550 and 800 G [1]. Model M2004 is quite accurate at fields below 100 G, but at higher fields its predictions are in error by up to ≈1%, or 8 G for B on the order of 800 G. This is not accurate enough to describe the scattering physics to sufficient precision to interpret the Efimov resonances, so an improved theoretical model is essential.

The aim of the present paper is to describe the properties of ^{133}Cs in its absolute atomic ground state in the magnetic

high-field region between 450 and 1000 G. We present new measurements of both resonance positions and binding energies at fields up to 1000 G. We then use these results to develop an optimized theoretical model, which we call M2012, that is accurate at both high and low magnetic fields. This model provides an accurate predictive tool to map the scattering length $a(B)$ as a function of magnetic field B [29], which is difficult to measure directly. This mapping was key to interpreting the Efimov features reported in Ref. [18].

This paper is organized as follows. Section II describes the essential molecular physics of threshold Cs states and describes the notation we use. Section III describes our experimental methods and results in the high-field region. Section IV describes our theoretical model. Section V describes our least-squares fits to the experimental results and compares experiment with theory in the regions of high, middle, and low fields. Section VI summarizes our conclusions.

II. NEAR-THRESHOLD STATES OF CESIUM DIMER

Two alkali-metal atoms in ^2S states interact at short range to form singlet ($X\,^1\Sigma^+$) and triplet ($a\,^3\Sigma^+$) states, with potential curves as shown in Fig. 1. Levels that lie more than about 100 GHz below dissociation have fairly well-defined singlet or triplet character, so lie principally on one or the other of these curves. However, the levels of primary interest in the present work are very close to dissociation and are bound by less than 1 GHz (and sometimes as little as 10 kHz). In this region the singlet and triplet states are strongly mixed by hyperfine interactions and it is more appropriate to describe the levels in terms of atomic quantum numbers.

The zero-field levels of the Cs atom are characterized by the nuclear spin $i = 7/2$, the electron spin $s = 1/2$, and their resultant $f = 3$ or 4, with the $f = 4$ level 9.19 GHz above $f = 3$. In a magnetic field B, each level splits into $2f + 1$ sublevels labeled by m_f, with the ground state $(f,m_f) = (3,+3)$. In the present work we label the atomic states with letters a,b,c, ... in increasing order of energy.

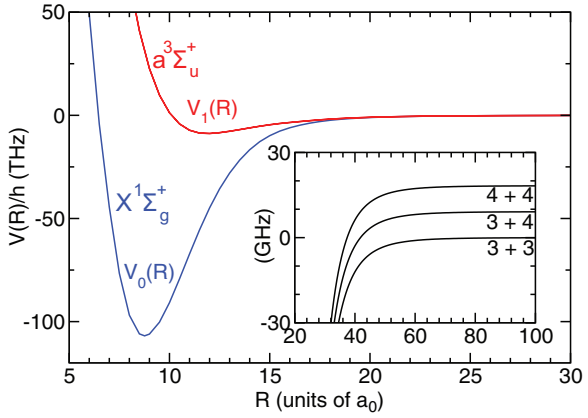

FIG. 1. (Color online) Molecular potential energy curves $V_0(R)$ and $V_1(R)$ for the singlet and triplet states of Cs_2. The inset shows an expanded view of the long-range potentials separating to the two different $f = 3$ and 4 hyperfine states of the atoms at magnetic field $B = 0$.

For Cs_2 there are three field-free atomic thresholds, labeled in increasing order of energy by $(f_1, f_2) = (3,3)$, (3,4), and (4,4), as shown in the inset of Fig. 1. In a magnetic field, each threshold splits into sublevels labeled by $(f_1,m_1) + (f_2,m_2)$. The near-threshold molecular states are to a good approximation described by quantum numbers (f_1, f_2, F, M_F), where F is the resultant of f_1 and f_2 and $M_F = m_1 + m_2$ (though m_1 and m_2 are not individually conserved). M_F is a nearly good quantum number except near avoided crossings. For a homonuclear molecule such as Cs_2, F is also nearly conserved in the region where the atomic Zeeman effect is near linear. Additional quantum numbers are needed for the molecular vibration n and the partial-wave angular momentum L. For near-dissociation levels it is convenient to specify n with respect to dissociation, so that the topmost level is $n = -1$, the next is $n = -2$, etc. In the present work we describe near-threshold levels using a set of quantum numbers $n(f_1 f_2)FL(M_F)$, with $L = 0,2,4$, etc. indicated by the usual labels s, d, g, etc. This is sometimes abbreviated to $FL(M_F)$ to avoid repetition. Following Ref. [1], we speak of bound levels with dominant s character in their wave function as s-wave levels; similarly for d- or g-wave levels with dominant $L = 2$ or 4 character in their wave functions.

Each molecular level lies within a "bin" below its associated threshold, with the boundaries of the bins determined by the long-range forces between the atoms. For Cs_2, with $V(r) = -C_6 r^{-6}$ at long range and $C_6 \approx 6890\ E_h a_0^6$ for both the singlet and triplet states, the $n = -1$ level lies between 0 and -105 MHz, and the $n = -2$ level lies between -105 and -725 MHz [1]. Similarly, bin boundaries can be worked out for more deeply bound levels. For Cs_2 the background scattering length for each channel is large and positive, on the order of the scattering length of the triplet potential. Under these circumstances all the levels lie near the top of their respective bins, and their energies E are approximately given by those of the triplet Born-Oppenheimer potential. Numerically, E/h is -0.0046 , -0.11, -0.75, -2.4, -5.5, -10.6, and -18.1 GHz for $n = -1$ to -7 for the M2004 model [9].

Feshbach resonances occur where a weakly bound state exists at the same energy as the colliding atoms. Zero-energy Feshbach resonances thus occur at magnetic fields where a bound state crosses an atomic threshold. Each resonance is labeled by the quantum numbers of the bound state that causes it. We work here with the scattering and bound states associated with the aa entrance channel, with two atoms in state a with $(f_1,m_1) = (3,+3)$. The energy zero at any magnetic field strength B is set to the energy of two a-state atoms. In s-wave scattering, the projection of the total angular momentum onto the field, $M_{\rm tot}$, is thus always +6 and is a rigorously conserved quantity. The left-hand panels of Fig. 2 show the s-wave bound states with $M_{\rm tot} = M_F = +6$ at magnetic fields up to 1000 G, together with the scattering length calculated using only s functions and thus including only resonances due to bound states with $L = 0$.

The $(f_1, f_2) = (3,3)$ levels with $M_F = +6$ in Fig. 2 have the same magnetic moment as the separated aa atoms, and thus the energies of these bound states are parallel to the $E = 0$ axis. However, $M_F = +6$ levels arising from other (f_1, f_2) combinations, and (3,3) levels with $M_F \neq +6$, have different

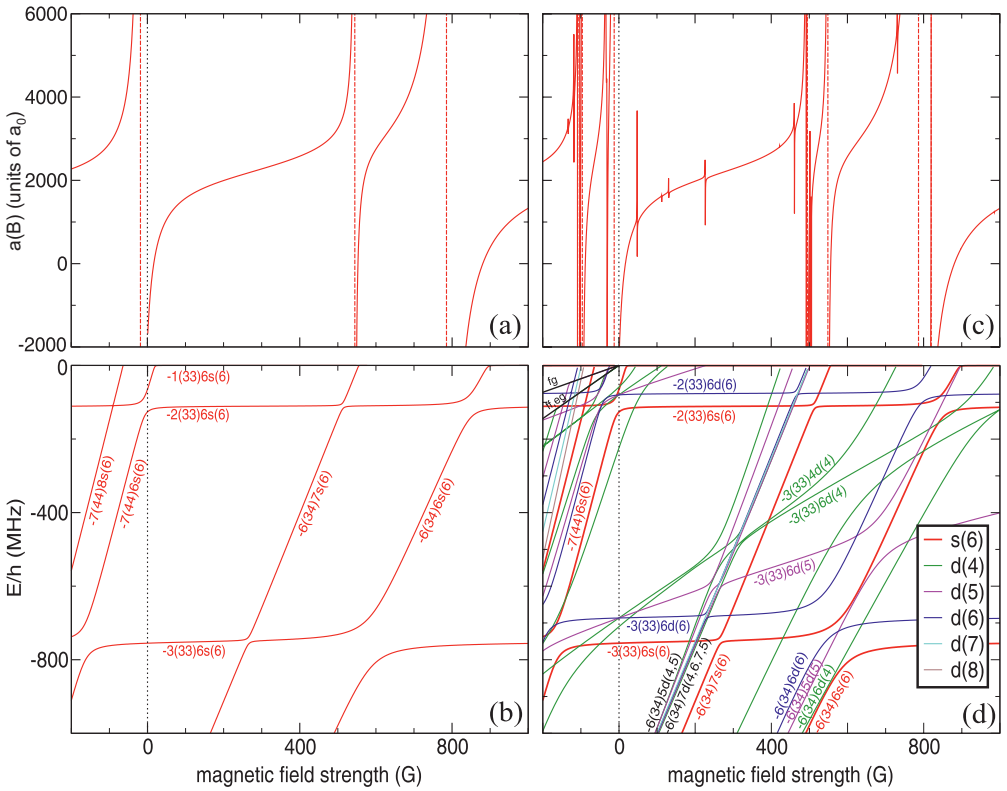

FIG. 2. (Color online) Scattering length and energy levels versus magnetic field B for Cs collisions in the lowest energy aa spin channel. (a) Scattering length, calculated including only s basis functions. The vertical lines indicate the pole positions. (b) Cs_2 s-wave bound-state energies below the aa threshold with $M_{\rm tot} = +6$, $M_F = +6$ in the range $B = -200$ to 1000 G, calculated with s basis functions only. (c) Scattering length, calculated including s and d basis functions and including all matrix elements of the spin-dipolar coupling. (d) Cs_2 s-wave and d-wave bound-state energies below the aa threshold with $M_{\rm tot} = +6$ and all allowed values of M_F in the range $B = -200$ to 1000 G. The legend shows the $L(M_F)$ labels. Levels with different L or M_F cross since small off-diagonal spin-dipolar matrix elements coupling them were not included in the calculation. Properties in the aa channel at negative values of B apply to the gg channel with reversed $M_{\rm tot} = -6$ (see text). The lines in the upper left corner of panel (d) show the energies of the fg, ff, and eg atomic channels.

magnetic moments and can cross the aa threshold as the magnetic field is varied. The three strong s-wave resonances at fields below 1000 G are associated with ramping $n(f_1 f_2)FL(M_F)$ states of $-7(44)6s(6)$, $-6(34)7s(6)$, and $-6(34)6s(6)$ character. However, it should be noted that in each case the ramping s-wave state mixes strongly with the least-bound state $-1(33)6s(6)$, which has a binding energy near 50 kHz, and this mixed state crosses threshold (and causes a pole in the s-wave scattering length) at a magnetic field below the field where the unperturbed ramping s-wave state would cross threshold. Such shifts in pole position are discussed in Refs. [1,30,31].

Figure 2 extends to negative magnetic field. This is to be interpreted as a reversal of axis, which is equivalent to changing the sign of all spin projection quantum numbers. Thus, the aa channel at $-|B|$ is equivalent to the gg channel at $+|B|$, where the gg channel has two g-state atoms $[(f_1, m_1) = (3, -3)]$. The bound states and scattering length are continuous across $B = 0$, and in particular the low-field behavior of the scattering length is largely due to the ramping $-7(44)6s(6)$ state, which actually produces a resonance around $B = -12$ G (i.e., in the gg channel), as shown in detail in Fig. 3.

Each s-wave bound state has a corresponding d-wave state, also with $M_F = +6$, that lies almost parallel to it but is shifted by the rotational energy of the vibrational state concerned; the rotational energy increases with binding energy and thus depends strongly on the vibrational quantum number n. However, levels with $L > 0$ and projection M_L such that $M_{\rm tot} = M_F + M_L = +6$ will also cross the aa threshold and can contribute to s-wave threshold scattering [32]. The bottom-right panel of Fig. 2 shows the bound-state energies including the additional d-wave levels with $M_F \neq 6$. The top-right panel shows the s-wave scattering length obtained with a basis set including both s and d functions (which we refer to as an sd basis set), showing the additional resonances that occur. Figure 3 shows an expanded view of the scattering length and near-threshold bound states calculated with an sd basis set in the low-field region between -60 and +60 G. Figure 4 shows the near-threshold g-wave bound states, as studied in Refs. [9,14,32].

Previous work on ultracold Cs has focused on the low-field region. The first experimental studies of the collisional properties of Cs were performed at Paris [12,33,34], Oxford [35,36], and Stanford [6–8]. Chin *et al.* [7] and Leo *et al.* [10] studied more than 30 resonances in several spin channels at fields below 130 G. Chin *et al.* [9] observed more than 60 resonances in eight different spin channels (aa, gg, hh, an, ao, ap, hn, and gf) for fields up to 250 G. In recent years,

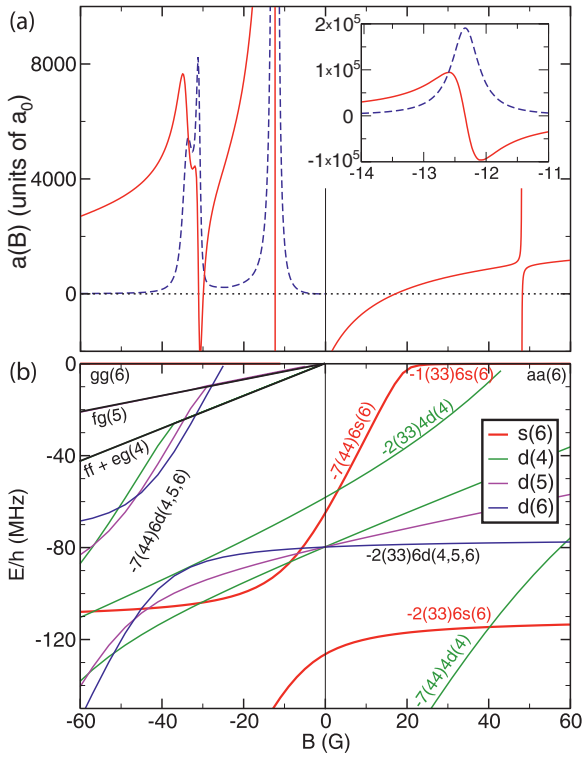

FIG. 3. (Color online) (a) The real (red, solid) and imaginary (blue, dashed) parts of the complex scattering length (see Sec. IV), calculated with an sd basis set. For $B < 0$, two-body relaxation is possible to channels fg, ff, or eg. The inset shows an expanded view of the pole region of the resonance near -12 G, indicating a maximum variation in scattering length of $\approx\pm 10^5\ a_0$ due to resonance decay. Panel (b) shows the bound states below threshold, calculated as in Fig. 2 so that levels of different L or M_F cross instead of showing avoided crossings. The M_F labels in the negative B regions are shown with reversed sign.

we have explored the energy spectrum of weakly bound Cs_2 Feshbach molecules by magnetic moment, microwave [14],

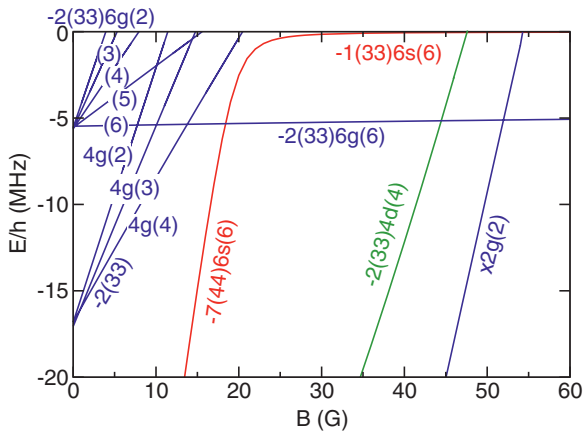

FIG. 4. (Color online) Low-field near-threshold bound levels of s, d, and g symmetry. As for Figs. 2 and 3, the avoided crossings between states of different L or M_F are not calculated because spin-dipolar coupling is omitted in this calculation. The low-field g-wave levels are of $-2(33)$ character, whereas the level marked $x2g(2)$ is of mixed $n(f_1 f_2) = -2(33)$, $-6(34)$, and $-7(44)$ character.

and magnetic field modulation spectroscopy [37]. The zero crossing of the s-wave scattering length was also precisely determined, using an approach based on measuring the interaction-induced dephasing of Bloch oscillations [38,39].

III. FESHBACH SPECTROSCOPY AT HIGH MAGNETIC FIELD

In the present work, we carry out a variety of different experiments on ultracold ^{133}Cs in its lowest internal state, $(f,m_f) = (3,3)$, at magnetic fields in the range between 450 and 1000 G. We first discuss the main experimental procedures and conditions (Sec. III A). Next we report on trap-loss spectroscopy, which allows measurement of the positions of narrow Feshbach resonances (Sec. III B). Finally we present magnetic field modulation spectroscopy for the precise determination of molecular binding energies near broad Feshbach resonances (Sec. III C).

A. Sample preparation

To access the high-field region, we have implemented a new magnetic-field system in the experimental setup [40]. This system is able to reach maximum magnetic field strengths up to 1400 G in a steady-state condition with 10 mG long-term stability. The high magnetic bias fields are created by three separately controllable pairs of magnetic field coils, made of 4- and 6-mm square-profile copper tubes insulated by glass-fiber braided sleevings. For each coil pair the electric currents, which are up to 400 A (4-mm tube) and 800 A (6-mm tube), respectively, are supplied by two 6-kW power supplies, connected in parallel. The temperature of the coil system is kept below 50 °C by internal water cooling of the copper tubes using a 10-bar pump system. Magnetic field stability is governed by controlling the current in the coils by an active feedback system, which operates at a precision level of 10^{-5}. For this, the actual currents are measured by highly sensitive current transducers. We have checked that precise current control is sufficient for magnetic field control to the limit given above. Other influences, such as thermal expansion of the copper coils, play a minor role. A detailed description of the magnetic-field coil system can be found in Ref. [40].

The procedure used to prepare an ultracold cesium sample in the absolute atomic ground is based on well-established cooling and trapping techniques, which are similar to the ones described in Ref. [41] down to the μK regime. After Zeeman slowing and cooling in a magneto-optical trap, the atoms are loaded into a three-dimensional optical lattice created by four laser beams, where Raman-sideband cooling [42–44] is performed for 3.5 ms. During this stage, where a small magnetic field of several hundred mG is applied, the atoms are cooled and spin-polarized into the absolute ground state. After Raman-sideband cooling the ensemble size amounts to 1.5×10^7 atoms at a temperature of about 1 μK. Then, the atoms are transferred into a large-volume far-off-resonant dipole trap [45] generated by two crossed 100-W CO_2 laser beams, featuring a waist of about 600 μm each. As the optical trap is not strong enough to hold the atoms against gravity, an additional magnetic levitation field of 31 G/cm is applied [13].

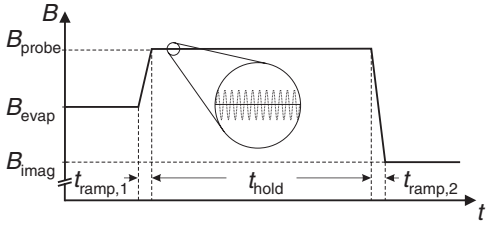

FIG. 5. Timing sequence for the magnetic field ramps for trap-loss spectroscopy and binding energy measurements. The magnetic field strength B is linearly ramped from the final evaporation field B_{evap} within the ramping time $t_{\mathrm{ramp},1}$ to the probe field B_{probe}. After an experimentally optimized hold time t_{hold} ranging between 0.2 and 1 s, the magnetic field strength is (linearly) ramped to the imaging field B_{imag}. For Scheme A, B_{evap} and B_{imag} are in the magnetic low-field region. The magnified segment visualizes B_{probe}, which is constant in time for trap-loss spectroscopy (solid line) and sinusoidally modulated for the determination of binding energies (dashed line).

We use two different schemes, which we refer to as *Scheme A* and *Scheme B*. Scheme A is based on evaporation and detection at low magnetic fields, similar to our previous work [14]. This scheme could be implemented in a simple way, but ramping up to the high probe field and back down to the detection field involves crossing several Feshbach resonances, which causes additional losses and heating. In the course of performing the present experiments, we developed an improved approach (Scheme B) that allows imaging in the magnetic high-field region and optimization of evaporative cooling at higher fields. In the following, both schemes are described in detail. Figure 5 illustrates the generic timing sequence for both schemes.

In Scheme A, evaporation is performed for 2 s at constant depth of the CO_2 laser trap in the magnetic low-field region. This stage of plain evaporation results in $\approx 5 \times 10^6$ atoms at a temperature slightly below 1 μK. Then, the CO_2 laser trap is spatially overlapped with a crossed dipole trap created by a 1064-nm fiber laser, with waists of 40 and 250 μm. To continue evaporation, the tightly focused 40-μm beam is ramped down from 60 to 3.5 mW within 6.5 s, while the intensity of the 250-μm beam is fixed at 400 mW. During this procedure, both CO_2 laser beams are switched off, finishing the sample transfer. The s-wave scattering length is large and positive during the evaporation sequence and is adjusted for the final evaporation step to $a \approx 200a_0$, corresponding to a magnetic field strength of $B_{\mathrm{evap}} \simeq 21$ G. Efficient evaporation conditions are encountered at this field because of an Efimov-related three-body recombination loss minimum [17]. In this way, we end up with 10^5 thermal atoms at a temperature of 70 nK in the magnetic low-field region.

When ramping over the broad Feshbach resonances, sizable effects of three-body recombination are unavoidable, even when applying the fastest possible ramp speeds. This causes direct recombination losses and additional heating [46], which can cause subsequent evaporation losses in the measurement process. To avoid the latter effect, we recompress the trap by increasing the intensity of the 40-μm beam by about a factor 10 before the magnetic field ramp is carried out. In the final step of the sample preparation, the levitation field is decreased to 8 G/cm. The mean trap frequency is about $\bar{\omega} = 2\pi \times 46(5)$ Hz, and the final sample contains 10^5 thermal atoms at a temperature of 120 nK in the magnetic low-field region.

The measurements are performed by linearly ramping from B_{evap} within a ramp time $t_{\mathrm{ramp},1} = 10$ ms to the probe fields B_{probe} in the magnetic high-field region. As described above, crossing of the broad s-wave Feshbach resonances leads to considerable heating of the sample and additional particle loss. We estimate the temperature at B_{probe} to be between 150 and 200 nK with Scheme A.

To determine the particle number, we linearly decrease the magnetic bias field to zero ($B_{\mathrm{imag}} \simeq 0$) within $t_{\mathrm{ramp},2} = 10$ ms and carry out resonant absorption imaging. The temperature is obtained in time-of-flight expansion measurements after release from the trap. The magnetic field strength is determined from measurements of the $(3,3) \rightarrow (4,4)$ microwave transition frequency by applying the Breit-Rabi formula [47].

In Scheme B, after loading the atoms from the Raman lattice to the levitated CO_2 laser trap, the magnetic field is linearly ramped to the magnetic high-field region within 10 ms. For measurements performed below 800 G the ramp ends at 561 G ($a = 1090a_0$), whereas for measurements above 800 it ends at 970 G ($a = 1140a_0$).

At this stage, the three-body recombination losses that are encountered while crossing the broad s-wave Feshbach resonances are limited because of the low density and the relatively high temperature ($T \simeq 1$ μK) of the sample. The temperature dependence of losses follows from the unitarity limitation of three-body recombination rates [48]. To compensate for the small change in the magnetic moment that is encountered during the ramp as a consequence of the quadratic contribution to the Zeeman effect, the magnetic levitation field is adjusted simultaneously. Then, 2 s of plain evaporation results in $\approx 5 \times 10^6$ atoms at a temperature of about 1 μK (similar to Scheme A). Then the CO_2 laser trap is spatially overlapped with the 1064-nm crossed dipole trap as described in Scheme A.

In the crossed dipole trap, we perform forced evaporation by decreasing the laser intensity of the 40-μm beam from 60 to 3.5 mW within 15 s. During this step, the intensity of the 250-μm beam is changed only slightly, from 400 to 300 mW. Both CO_2 lasers are switched off during the first 5 s of evaporation to achieve an efficient transfer to the 1064-nm trap. The magnetic bias field is adjusted during the evaporation sequence for optimized elastic scattering conditions. The last evaporation step of this sequence ends at $B_{\mathrm{evap}} = 558.7$ G ($a \approx 700a_0$) or $B_{\mathrm{evap}} = 894$ G ($a \approx 300a_0$), respectively. Note that close to 894 G an Efimov-related recombination minimum is present [18], which apparently facilitates efficient evaporation. After recompression and reshaping, leading to a mean trap frequency of $\bar{\omega} = 2\pi \times 26(3)$ Hz, we end up with a noncondensed sample of between 5×10^4 and 10^5 atoms at a temperature of about 50 nK.

For Scheme B, no broad s-wave Feshbach resonances are crossed in the final magnetic field ramps to reach B_{probe}, and therefore no noteworthy heating effects and particle losses are observed. The particle number is determined by high-field imaging in the vicinity of the zero crossing of the broad s-wave Feshbach resonances at $B_{\mathrm{imag}} = 556.4$ G

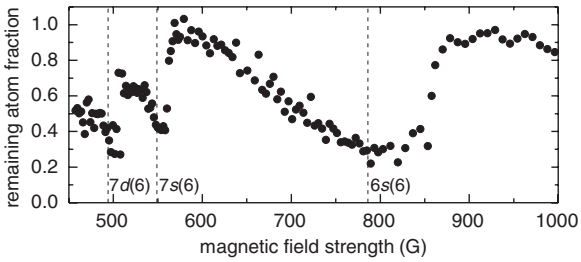

FIG. 6. Results of trap-loss spectroscopy in the magnetic field region between 450 and 1000 G, performed with Scheme B. The enhancements in losses result from broad Feshbach resonances centered at 494, 549, and 787 G. The resonance positions, which are derived from our theoretical model (see Sec. IV), are indicated by dashed lines, labeled according to the quantum numbers $FL(M_F)$ of the molecular states that cause the resonances. The measurements are performed with a hold time of 500 ms. Narrow Feshbach resonances are not visible in this scan because of the large step size of about 2 G. A remaining atom fraction of 1.0 corresponds to 8×10^4 atoms.

and $B_{\mathrm{imag}} = 887.5$ G. The magnetic field ramps to and from B_{probe} involve linear changes of the magnetic field with $t_{\mathrm{ramp},1} = t_{\mathrm{ramp},2} = 10$ ms, as for Scheme A. The procedures for magnetic field calibration and temperature determination are the same as the ones in Scheme A.

B. Trap-loss spectroscopy

Trap-loss spectroscopy is a well-established method based on the enhancement of collisional losses in the vicinity of a Feshbach resonance [1]. For atoms in the absolute atomic ground state, where inelastic binary collisions are energetically forbidden, three-body recombination is the lowest-order loss process. In this process three colliding atoms recombine to a molecule and a free atom. Typically, the kinetic energy released far exceeds the trapping potential, leading to loss of the three particles involved. The general a^4 scaling of three-body recombination rates [46,49–51] leads to a maximum in losses at the magnetic field position B_{max}, corresponding to the divergence of a at the Feshbach resonance pole, and a minimum at the position B_{min}, close to the zero crossing of the s-wave scattering length. This allows the observed losses to be directly related to the positions and widths of the Feshbach resonances.

In this section, we first report on experiments characterizing the scattering properties in the vicinity of the broad s-wave Feshbach resonances, as shown in Fig. 2(a), by performing a broad magnetic field scan with large step size. Then, we decrease the step size to perform detailed scans to identify and characterize narrow Feshbach resonances, which originate from states with higher rotational angular momentum ($L > 0$).

Trap-loss spectroscopy is performed by recording the remaining atom fraction after a hold time t_{hold} at the probe field B_{probe}. In general, we cannot exclude additional losses encountered within $t_{\mathrm{ramp},1}$ and $t_{\mathrm{ramp},2}$ during the magnetic field ramps $B_{\mathrm{evap}} \rightarrow B_{\mathrm{probe}}$ and $B_{\mathrm{probe}} \rightarrow B_{\mathrm{imag}}$. However, for the characterization of narrow Feshbach resonances only a small magnetic field region is investigated, where variations in the initial atom number are negligible. Furthermore, the measurements are performed with $t_{\mathrm{hold}} \gg t_{\mathrm{ramp},1}, t_{\mathrm{ramp},2}$, strongly limiting the effect of finite ramp times.

The broad scan of the magnetic high-field region covers a range from 450 to 1000 G, as shown in Fig. 6. This scan clearly shows two broad loss features around 550 and 800 G, which can be assigned to the two high-field s-wave Feshbach resonances, as discussed in Sec. II (see top panels Fig. 2). These measurements demonstrate the large width of the Feshbach resonance near 800 G. Because of the unitarity limitation of three-body recombination losses [48], it is not possible to determine B_{max} accurately for the s-wave resonances by trap-loss spectroscopy.

In the region around 500 G, no s-wave Feshbach resonance is expected, but the theoretical model predicts a series of closely adjoining d-wave Feshbach resonances, as shown in Fig. 2. One of these has a width of about 5 G, producing the broad loss signal around 495 G seen in Figs. 6 and 7.

We perform high-resolution scans by decreasing the step size of the magnetic field scans to a few mG. The results of these scans are displayed in Fig. 7. We observe 15 narrow loss

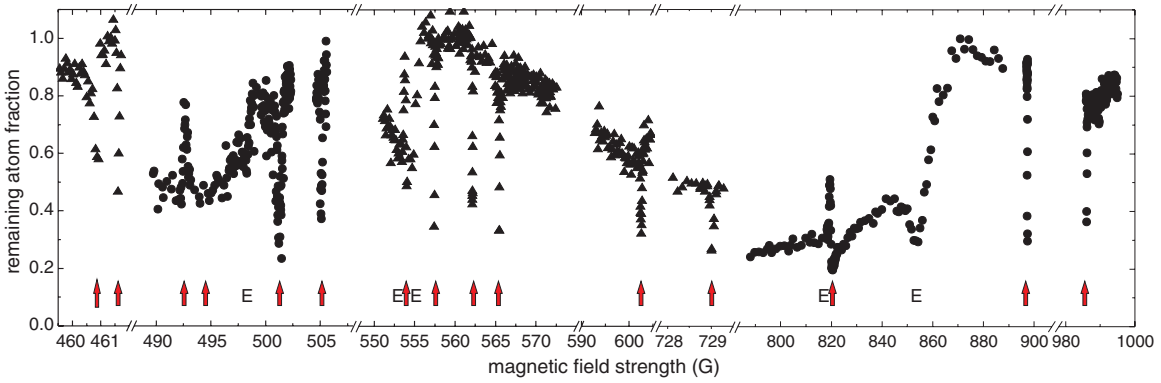

FIG. 7. (Color online) Detailed results of trap-loss spectroscopy in the magnetic high-field region. We observe 15 Feshbach resonances, stemming from d-, g-, and i-wave molecular states. Measurements indicated by (▲) symbols are obtained by Scheme A, whereas the (●) symbols refer to data points acquired with Scheme B. The poles of the Feshbach resonances, omitting the s-wave resonances, are marked with an arrow. The loss features at 498.1, 553.3, 554.7, 818.9, and 853.1 G, which are indicated by "E", are related to Efimov loss resonances as reported in Refs. [18,52]. Note that the data in the intervals [728,729.5] and [980, 1000] G, which are measured for different t_{hold}, are multiplied by scaling factors of 0.5 and 0.9, respectively, to reproduce the overall behavior shown in Fig. 6. A remaining atom fraction of 1.0 corresponds to 8×10^4 atoms.

TABLE I. Results of trap-loss spectroscopy in the magnetic high-field region. The table shows the magnetic field values for loss maxima (B_{max}), resulting from the poles of the Feshbach resonances, and minima (B_{min}), which are related to the zero crossings of the s-wave scattering length. The numbers in brackets are the experimental 1σ uncertainties, including statistical and systematic errors. The assignments of the Feshbach resonances identify the molecular states that cause the resonances. In the case of very narrow resonances, the zero crossings could not be determined experimentally.

Molecular state $n(f_1 f_2)FL(M_F)$	B_{max} (G)	B_{min} (G)
$-6(34)5d(5)$	460.86(5)	
i wave[a]	461.62(5)	
$-6(34)7$[b]	492.45(3)	492.63(3)
$-6(34)7$[b]	494.4(9)	499.4(1)
$-6(34)7$[b]	501.24(3)	
$-6(34)7$[b]	505.07(3)	
$g(3)$[c]	554.06(2)	553.73(2)
i wave[a]	557.45(3)	
i wave[a]	562.17(3)	
$g(4)$[c]	565.48(3)	
$-2(33)6g(6)$[d]	602.54(3)	
$g(5)$[c]	729.03(3)	
$-6(34)6d(6)$	820.37(20)	819.41(2)
$-6(34)5d(5)$	897.33(3)	
$-6(34)6d(4)$	986.08(3)	

[a]For the i-wave resonances only the L quantum number of the molecular state is known.

[b]These Feshbach resonances arise from d-wave molecular states with $M_F = 4, 5, 6,$ and 7, which are strongly mixed at the atomic threshold. Therefore, we cannot give simple M_F quantum numbers and use "x" to indicate the strong coupling.

[c]For these states only the quantum numbers L and M_F are known.

[d]This molecular state is strongly mixed with the state $-6(34)6g(6)$.

features, which can be assigned according to the theoretical model given in Sec. IV to Feshbach resonances originating from the coupling of the free atoms to molecular states with rotational angular momentum $L > 0$.

We observe three narrow resonances that cannot be attributed to s-, d-, or g-wave molecular states in the present model. They are found at 461.62, 557.45, and 562.17 G. Our model, however, predicts the existence of Feshbach resonances stemming from i-wave molecular states ($L = 6$) in the magnetic field regions where we observe these features. The calculations are not accurate enough to establish an unambiguous assignment, but the match between experiment and theory nevertheless provides strong evidence that this is experimental observation of i-wave Feshbach resonances, which have not previously been reported. These resonances are discussed further in Sec. IV.

The positions of the poles of the d-, g-, and i-wave Feshbach resonances obtained in these measurements are summarized in Table I. The peak positions are determined by Gaussian fits to the loss peaks. For several of these resonances we also identify recombination loss minima, which also provide estimates for the corresponding resonance widths.

Figure 8 shows expanded views of two regions in Fig. 7, where interesting cases of overlapping FR scenarios occur.

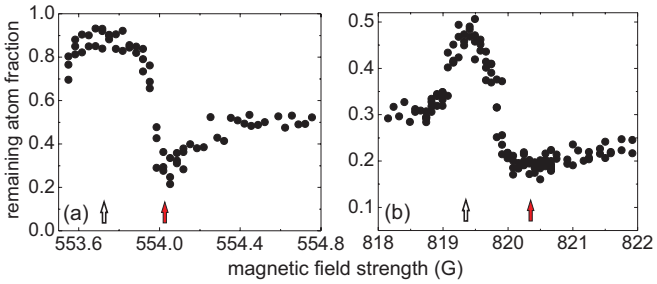

FIG. 8. (Color online) Expanded view of Fig. 7, showing the Feshbach resonances arising from the $g(3)$ state (a) and the $-6(34)6d(6)$ state (b), which overlap with the broad s-wave resonances. The solid and open arrows mark the poles and zero crossings of the scattering length, respectively. The remaining atom fraction at the zero crossing in (b) is limited due to losses during the magnetic field ramps.

Figure 8(a) shows a g-wave resonance centered at 554.06(2) G sitting on the shoulder of the 549-G s-wave Feshbach resonance at a background scattering length of about $-1000a_0$. The zero crossing of $a(B)$ leads to a loss minimum at 553.73(2) G. Even more intriguing is a d-wave Feshbach resonance situated at 820.4(2) G. There, the broad 787-G s-wave Feshbach resonance leads to an extremely large background scattering length of about $-4200a_0$. Experimentally, this large background masks the loss maximum but clearly reveals the zero crossing at 819.41(2) G, as shown in Fig. 8(b). Both the g-wave and the d-wave resonance have rather large widths, of 0.33(3) and 0.96(22) G, respectively. Efimov-related three-body physics has been revealed in the vicinity of these resonances, as reported in Refs. [18,52].

C. Binding energy measurements

Binding energy measurements of weakly bound dimer states provide a powerful additional tool to extract information on the cesium interaction potentials and scattering properties. In particular, for the s-wave Feshbach resonances the exact positions of the poles are obscured by strong loss across a broad magnetic field range, but can be extracted accurately from binding energies. In the present work, we measure the binding energies by magnetic field modulation spectroscopy, a method which was introduced in Ref. [53]. This method is based on a sinusoidal modulation of the magnetic bias field and allows the creation of dimers starting from an ultracold atom sample. This leads to an observable loss signal due to fast atom-dimer relaxation when the modulation frequency matches the binding energy of the dimers plus the small relative kinetic energy of the colliding atoms. Since the modulation of the magnetic field is parallel to the magnetic bias field, only transitions between states with the same projection quantum number of the total angular momentum are observed. This procedure has been successfully applied in several experiments [37,53–58] to determine atomic scattering properties.

The atom samples for the binding energy measurements are prepared according to Scheme B, as described in Sec. III A. At B_{probe}, a modulation signal is applied for a variable duration of $t_{hold} = 0.1$ to 1 s, in a frequency range of 50 to 1600 kHz and an amplitude between 0.5 and 3 G (see Fig. 5). The amplitude and the duration of the pulse are experimentally adjusted for each

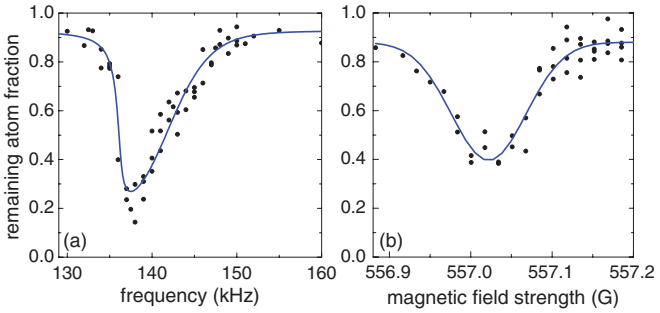

FIG. 9. (Color online) Typical signals for magnetic field modulation spectroscopy. (a) Frequency scan at a fixed magnetic field strength of 911.69 G. The asymmetric shape of the signal is fitted by a model that takes the temperature of the sample into account [59]. (b) Magnetic field scan at a constant modulation frequency of 425 kHz, revealing a loss resonance at 557.02 G. This resonance stems from the s-wave molecular state. The line represents a Gaussian fit. A remaining atom fraction of 1.0 corresponds to (a) 4.5×10^4 and (b) 2.5×10^4 atoms.

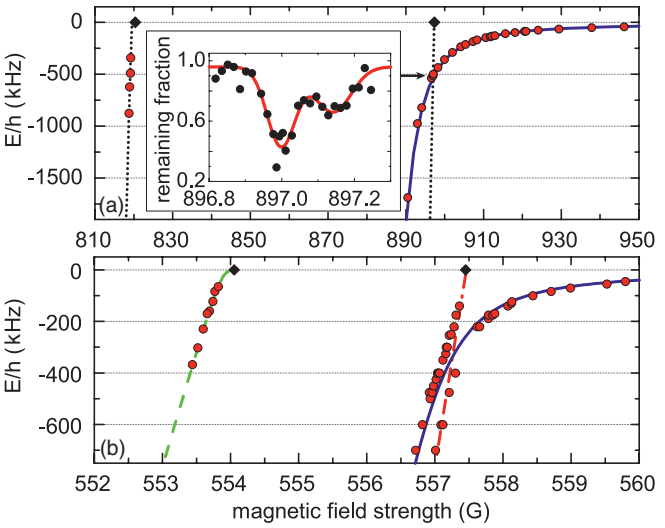

FIG. 10. (Color online) Results of experimental binding energy measurements. (a) The $-6(34)6d(6)$ and $-6(34)5d(5)$ states (dashed lines) and the $-6(34)6s(6)$ state (solid line) between 820 and 950 G. The lines are guides for the eye. The inset shows a binding energy measurement at the crossing of the $-6(34)6s(6)$ and $-6(34)5d(5)$ states at 509 kHz. At fields above 900 G the s-wave state takes on the character of the least-bound state $-1(33)6s(6)$, which has a binding energy around $h \times 50$ kHz away from avoided crossings. The strong variation of the magnetic moment follows from the avoided crossing with this threshold s-wave state. (b) The binding energies of the $g(3)$ state (dashed line), an i-wave state (dot-dash line), and the $-6(34)7s(6)$ state (solid line). The positions of the resonance poles are marked by a (⧫) symbol, with values taken from Table I.

binding energy measurement to optimize the signal-to-noise ratio. The signal is generated by a programmable frequency generator and subsequently amplified by a commercial 25-W radio-frequency amplifier, which drives the current in a separate set of coils and thereby creates the modulation of the magnetic bias field.

The measurements are usually performed by varying the modulation frequency at a fixed B_{probe}. Another possibility, however, is to scan B_{probe} while the modulation frequency is kept constant. The advantage of the latter approach is that it is less sensitive to atom losses caused by technical imperfections, such as resonance phenomena in the electric circuit that drives the transitions. We checked that the two methods give consistent results in our measurements. Figure 9 shows sample loss signals derived in a frequency scan (a) and a magnetic field scan (b).

We studied the binding energies E_b of the high-field s-wave states and of several d-, g-, and i-wave states, as shown in Fig. 10. For the s-wave states with $E_b/h < 200$ kHz, we observed asymmetric line shapes resulting from the finite temperature of the samples. We include this effect in our fitting routine using the line-shape model of Ref. [59]. For s-wave states with $E_b/h > 200$ kHz and for dimer states with higher rotational angular momentum, the binding energy has a strong dependence on the magnetic field. In these cases, the magnetic field noise and the field gradient that is applied to levitate the atoms broaden and symmetrize the loss signals. For these symmetrized signals, the effect from the finite temperature plays a minor role, and we therefore obtain E_b by fitting a simple Gaussian distribution to the data.

In the binding energy measurements, we observe several avoided crossings between molecular states. Around 897 G and $E_b/h \approx 500$ kHz, the $-6(34)6s(6)$ state crosses the $-6(34)5d(5)$ state. These two states are clearly resolved as separate loss features in each magnetic field scan performed at fixed frequency in the crossing region, as shown in the inset of Fig. 10(a). In addition, we observe an avoided crossing at about 557 G and $E_b/h \approx 350$ kHz between the $-6(34)7s(6)$ state and an i-wave state, which clearly shows up in the binding energy measurements presented in Fig. 10(b).

In view of the large difference in the partial-wave angular momentum $\Delta L = 6$, the crossing around 557 G appears to be surprisingly strongly avoided. To confirm this, we prepare molecular samples in the s-wave state by Feshbach ramps [1] and perform magnetic moment spectroscopy for magnetic field strengths ranging from 556.5 to 557.5 G using the Stern-Gerlach effect in the same way as described in Ref. [14]. To do this, we release the dimers from the trap while the magnetic field gradient is switched on. After a fixed time of flight, the dimers are dissociated by ramping back over either the 557.45-G or the 565.48-G Feshbach resonance. Subsequently, the atoms are imaged and the molecular magnetic moment is extracted from the vertical position of the atom cloud. We observe a smooth change of the magnetic moment around 557.15 G over a magnetic field range of about 250 mG, indicating that the character of the molecular state also changes smoothly, from s-wave to i-wave character, over the width of the crossing. Because of large calibration uncertainties in these measurements, we cannot provide absolute values for the molecular magnetic moments. In another experiment, we start with weakly bound s-wave Feshbach molecules at a magnetic field of 560 G and attempt to jump the avoided crossing diabatically. As in the experiment previously outlined, we can simultaneously detect and distinguish s-wave and i-wave dimers by their magnetic moment. Applying a maximum ramp speed of 10 G/ms, the number of transferred dimers is below

our detection limit. This sets a lower limit of 30 kHz to the strength of the avoided crossing according to the Landau-Zener formula [60,61].

IV. THEORETICAL MODEL

The Hamiltonian for the interaction of two Cs atoms may be written

$$\frac{\hbar^2}{2\mu}\left[-R^{-1}\frac{d^2}{dR^2}R+\frac{\hat{L}^2}{R^2}\right]+\hat{h}_1+\hat{h}_2+\hat{V}(R), \qquad (1)$$

where μ is the reduced mass and $\hat{L}^2$ is the operator for the end-over-end angular momentum of the two atoms about one another. The monomer Hamiltonians including Zeeman terms are

$$\hat{h}_j=\zeta\hat{\imath}_j\cdot\hat{s}_j+g_e\mu_B B\,\hat{s}_{zj}+g_n\mu_B B\,\hat{\imath}_{zj}, \qquad (2)$$

where ζ is the atomic hyperfine constant, $\hat{s}_1$ and $\hat{s}_2$ represent the electron spins of the two atoms, and $\hat{\imath}_1$ and $\hat{\imath}_2$ represent nuclear spins. g_e and g_n are the electron and nuclear g factors, μ_B is the Bohr magneton, and $\hat{s}_z$ and $\hat{\imath}_z$ represent the z components of $\hat{s}$ and $\hat{\imath}$ along a space-fixed Z axis whose direction is defined by the external magnetic field B. The interaction between the two atoms $\hat{V}(R)$ is

$$\hat{V}(R)=\hat{V}^{\rm c}(R)+\hat{V}^{\rm d}(R). \qquad (3)$$

Here $\hat{V}^{\rm c}(R)=V_0(R)\hat{\mathcal{P}}^{(0)}+V_1(R)\hat{\mathcal{P}}^{(1)}$ is an isotropic potential operator that depends on the potential energy curves $V_0(R)$ and $V_1(R)$ for the respective X $^1\Sigma_g^+$ singlet and a $^3\Sigma_u^+$ triplet states of Cs_2, as shown in Fig. 1. The singlet and triplet projectors $\hat{\mathcal{P}}^{(0)}$ and $\hat{\mathcal{P}}^{(1)}$ project onto subspaces with total electron spin quantum numbers 0 and 1, respectively. The term $\hat{V}^{\rm d}(R)$ represents small, anisotropic spin-dependent couplings that are responsible for the avoided crossings discussed in the present paper and are discussed further in Sec. IV C below.

A. Computational methods for bound states and scattering

The present work solves the Schrödinger equation for both scattering and Feshbach bound states of Cs_2 by coupled-channel methods, using a basis set for the electron and nuclear spins in a fully uncoupled representation,

$$|s_1m_{s1}\rangle|i_1m_{i1}\rangle|s_2m_{s2}\rangle|i_2m_{i2}\rangle|LM_L\rangle, \qquad (4)$$

symmetrized to take account of exchange symmetry. The matrix elements of the different terms in the Hamiltonian in this basis set are given in the Appendix of Ref. [32]. The only rigorously conserved quantities are the parity, $(-1)^L$, and the projection of the total angular momentum, $M_{\rm tot}=m_{s1}+m_{i1}+m_{s2}+m_{i2}+M_L$. The calculations in this paper used basis sets with all possible values of m_s and m_i for both atoms that are consistent with the required $M_{\rm tot}$ and parity, truncated at $L_{\rm max}=4$ (an sdg basis set) unless otherwise indicated. All calculations in this paper are for s-wave incoming channels, so have even parity.

Both scattering and bound-state calculations use propagation methods and do not rely on basis sets in the interatomic distance coordinate R.

Scattering calculations are carried out using the MOLSCAT package [62], as modified to handle collisions in magnetic fields [63]. At each magnetic field B, the wave-function log-derivative matrix at collision energy E is propagated from $R_{\rm min}=6a_0$ to $R_{\rm mid}=20a_0$ using the propagator of Manolopoulos [64] with a fixed step size of $0.002a_0$, and from $R_{\rm mid}$ to $R_{\rm max}=4000a_0$ using the Airy propagator [65] with a variable step size controlled by the parameter TOLHI $=10^{-5}$ [66]. Scattering boundary conditions [67] are applied at $R_{\rm max}$ to obtain the scattering S matrix. The energy-dependent s-wave scattering length $a(k)$ is then obtained from the diagonal S matrix element in the incoming $L=0$ channel using the identity [68]

$$a(k)=\frac{1}{ik}\left(\frac{1-S_{00}}{1+S_{00}}\right), \qquad (5)$$

where $k^2=2\mu E/\hbar^2$.

In the vicinity of a resonance at the lowest atomic threshold, the scattering length as a function of magnetic field (at small fixed k) follows the functional form

$$a(B)=a_{\rm bg}[1-\Delta/(B-B_{\rm res})]. \qquad (6)$$

The resonance pole position $B_{\rm res}$ may be associated with the three-body loss maximum at a field $B_{\rm max}$. For a narrow resonance (where the background scattering length $a_{\rm bg}$ does not vary significantly across the resonance), the width Δ is conveniently obtained from the difference between the positions of the pole and zero in $a(B)$. Experimentally, this corresponds to the difference in field between the loss maximum at $B_{\rm max}$ and the loss minimum at $B_{\rm min}$. We have extended MOLSCAT to provide an option to *converge* on poles and zeros of $a(B)$, instead of extracting them from a fit to a grid of points.

Weakly bound levels for Feshbach molecules are obtained using a variant of the propagation method described in Ref. [32]. The log-derivative matrix is propagated outwards from $R_{\rm min}$ to $R_{\rm mid}$ with a fixed step size of $0.002a_0$ and inwards from $R_{\rm max}$ to $R_{\rm mid}$ with a variable step size, using the same propagators as for scattering calculations. $R_{\rm mid}=25a_0$ and $R_{\rm max}=4000a_0$ were used for most bound states, although $R_{\rm mid}=35a_0$ and $R_{\rm max}=8000a_0$ were needed for states within about 50 kHz of dissociation. In Ref. [32], bound-state energies at a fixed value of the magnetic field B were located using the BOUND package [69], which converges on energies where the smallest eigenvalue of the log-derivative matching determinant is zero [70]. However, for the purposes of the present work we used a new package, FIELD [71], which instead works at fixed binding energy and converges in a similar manner on the magnetic fields at which bound states exist. BOUND and FIELD both implement a node-count algorithm [70], which makes it straightforward to ensure that *all* bound states that exist in a particular range of energy or field are located.

As described above, zero-energy Feshbach resonances can, in principle, be located as the fields at which the scattering length $a(B)$ passes through a pole. However, with this method it is necessary first to search for poles, and it is quite easy to miss narrow resonances. However, since resonances occur at fields where there is a bound state at zero energy, the FIELD package provides a much cleaner approach: Simply running FIELD at zero energy provides a complete list of all fields at which zero-energy Feshbach resonances exist [29]. In the

present work we located resonances using FIELD and then obtained their widths by converging on the nearby zero in $a(B)$ using MOLSCAT.

B. Representation of the potential curves

At long range, the potentials are

$$V_S^{\rm LR}(R) = -C_6 y_6(R)/R^6 - C_8 y_8(R)/R^8 - C_{10} y_{10}(R)/R^{10} \pm V_{\rm ex}(R), \quad (7)$$

where $S = 0$ and 1 for singlet and triplet, respectively. The dispersion coefficients C_n are common to both potentials and the functions $y_n(R)$ account for retardation corrections [72]. The exchange contribution is [73]

$$V_{\rm ex}(R) = A_{\rm ex}(R/a_0)^\gamma \exp(-\beta_{\rm ex} R/a_0) \quad (8)$$

and makes an attractive contribution for the singlet and a repulsive contribution for the triplet. The value of $\beta_{\rm ex}$ is usually obtained from the ionization energies of the atoms [73], which for Cs gives $\beta_{\rm ex} = 1.069\,946$, and γ is related to β by $\gamma = 7/\beta - 1$. In the present work we found that, to reproduce the experimental results, it was necessary to reduce $\beta_{\rm ex}$ slightly from its original value. We therefore introduce an additional factor $\rho_{\rm ex}$ so that $\beta_{\rm ex} = 1.069\,946\rho_{\rm ex}$, with γ adjusted accordingly.

The detailed shapes of the short-range singlet and triplet potentials are relatively unimportant for the ultracold scattering properties and near-threshold binding energies considered here, although it is crucial to be able to vary the *volume* of the potential wells to allow adjustment of the singlet and triplet scattering lengths. In the present work we retained the functional form used by Leo *et al.* [10] and Chin *et al.* [9]. Each short-range potential is represented by a set of 14 *ab initio* points between $R = 7a_0$ and $20a_0$ [74]. The two sets of potential points are first multiplied by R^6 and the resulting (smoother) functions are interpolated using Akima splines [75] to obtain their values at $R_{\rm LR} = 17.6a_0$. The value of $A_{\rm ex}$ is chosen to match $V_{\rm ex}$ to $(V_1 - V_0)/2$ at $R_{\rm LR}$, and both sets of points are shifted to match $(V_1 + V_0)/2$ at $R_{\rm LR}$. Finally, the analytic $V_S^{\rm LR}(R)$ is used to generate new grid points between $17.6a_0$ and $20a_0$ and the resulting sets of points are reinterpolated as above between $R = 7a_0$ and $20a_0$. The analytic long-range form (7) is used outside $20a_0$.

The flexibility needed to adjust the singlet and triplet scattering lengths is provided by simply adding a quadratic shift to each of the singlet and triplet potentials inside its minimum,

$$V_S^{\rm shift}(R) = S_S(R - R_{eS})^2 \quad \text{for} \quad R < R_{eS}, \quad (9)$$

with $R_{e0} = 8.75a_0$ and $R_{e1} = 11.8a_0$.

C. Magnetic dipole interaction and second-order spin-orbit coupling

At long range, the coupling $\hat{V}^{\rm d}(R)$ of Eq. (3) has a simple magnetic dipole-dipole form that varies as $1/R^3$ [76,77]. However, for atoms as heavy as Cs, second-order spin-orbit coupling provides an additional contribution that has the same tensor form as the dipole-dipole term and dominates at short range [78]. In the present work, $\hat{V}^{\rm d}(R)$ is represented as

$$\hat{V}^{\rm d}(R) = \lambda(R)[\hat{s}_1 \cdot \hat{s}_2 - 3(\hat{s}_1 \cdot \vec{e}_R)(\hat{s}_2 \cdot \vec{e}_R)], \quad (10)$$

where $\vec{e}_R$ is a unit vector along the internuclear axis and λ is an R-dependent coupling constant. The second-order term has been calculated by Kotochigova *et al.* [79] and fitted to a biexponential form, so that the overall form of $\lambda(R)$ is

$$\lambda(R) = E_{\rm h}\alpha^2\left[A_{\rm 2SO}^{\rm short}\exp(-2\beta_{\rm 2SO}R) + A_{\rm 2SO}^{\rm long}\exp(-\beta_{\rm 2SO}R) + \frac{1}{(R/a_0)^3}\right], \quad (11)$$

where $\alpha \approx 1/137$ is the fine-structure constant and the parameters obtained from fitting to the electronic structure calculations [79] are $A_{\rm 2SO}^{\rm short}/hc = 34.4$ cm^{-1}, $A_{\rm 2SO}^{\rm long}/hc = 0.25$ cm^{-1}, and $\beta_{\rm 2SO} = -0.35a_0^{-1}$. However, in fitting to the experimental results, this coupling function was found to be slightly too strong. We therefore retained the functional form (11) but introduced an additional scaling factor $S_{\rm 2SO}$ that multiplies both exponential terms and is allowed to vary in the least-squares fit to the experimental results.

V. LEAST-SQUARES FITTING OF POTENTIAL PARAMETERS

In the present work, our primary objective is to obtain potential parameters that give a reliable representation of $a(B)$ in the regions where Efimov resonances occur, namely near 8, 554, and 853 G. Earlier potentials [9,10] focused on representing the positions of Feshbach resonances in the low-field region below about 60 G.

A key advantage of the propagator approach to locating bound states and resonances, implemented in the BOUND and FIELD programs, is that it is fast enough to be incorporated in a least-squares fitting program. We have therefore carried out direct least-squares refinement of the potential parameters. We experimented with fitting various combinations of parameters, and concluded that adequate flexibility is available in the six-parameter space S_0, S_1, C_6, C_8, $S_{\rm 2SO}$, $\rho_{\rm ex}$.

The set of experimental results used for fitting is listed in Table II. It consists of all the observed resonance positions (loss maxima) in the regions relevant to Efimov physics, together with representative bound-state positions. It also includes zero crossings of the scattering lengths measured from loss minima, Bloch oscillations [38], and BEC collapse measurements [80]. All the bound-state positions are expressed as the fields at which bound states exist at specific binding energies, except for the $-3(33)6g(6)$ state, which is almost parallel to the lowest threshold and is included in the fit as a binding energy at $B = 18.6$ G. The strength of the avoided crossing between the $-2(33)4d(4)$ and $-7(44)6s(6)$ states near 48 G is included as an explicit difference between fields where states exist at energies of 78 and 24 kHz. The quantity optimized in the least-squares fits was the sum of squares of residuals [(obs−calc)/uncertainty], with the uncertainties listed in Table II [81].

Although the experimental data do allow all six of the potential parameters described above to be determined, the fit is very highly correlated. Under these circumstances, a fully

TABLE II. Quality of fit between calculations using the M2012 model and the experimental results used in the fit.

	B_{obs} (G)	B_{calc} (G)	$B_{obs} - B_{calc}$ (G)	Unc. (G)	Method	Reference
$-7(44)6s(6)$ at 7.8 MHz	17.53	17.51	0.02	0.02	Microwave spectroscopy	[14]
$-7(44)6s(6)$ at 1.2 MHz	21.60	21.59	0.01	0.02	Microwave spectroscopy	[14]
$-7(44)6s(6)$ at 104 kHz	32.05	31.70	0.35	0.03	Magnetic field modulation	[37]
Zero crossing near 17 G	17.12	17.14	−0.02	0.01	Bloch oscillations	[38]
$-2(33)4d(4)$ at 174 kHz	48.01	48.01	0.00	0.06	Magnetic field modulation	[37]
$-2(33)4d(4)$ crossing strength 78–24 kHz	1.19	1.21	−0.02	0.02	Magnetic field modulation	[32]
Loss minimum (d) near 48 G	47.94	47.98	−0.04	0.04	Inferred from magnetic field modulation	[37]
Loss maximum (d) near 48 G	47.78	47.79	−0.01	0.06	Inferred from magnetic field modulation	[37]
Δ (d) near 48 G	0.16	0.18	−0.02	0.06	Inferred from magnetic field modulation	[37]
$2g(2)$ at 17 kHz	53.42	53.76	−0.34	0.08	Magnetic field modulation	[37]
$-2(33)6g(6)$ at 18.6 G (MHz, not G)	−5.03	−4.99	−0.04	0.01	Microwave spectroscopy	[14]
Loss maximum $-6(34)7d(x)$	492.45	492.68	−0.23	0.06	Trap loss spectroscopy	This work
Loss maximum $-6(34)7d(x)$	501.24	501.44	−0.20	0.06	Trap loss spectroscopy	This work
Loss maximum $-6(34)7d(x)$	505.07	505.37	−0.30	0.06	Trap loss spectroscopy	This work
$-6(34)7s(6)$ at 1.0 MHz	556.47	556.48	−0.01	0.02	Magnetic field modulation	This work
$-6(34)7s(6)$ at 700 kHz	556.72	556.76	−0.04	0.02	Magnetic field modulation	This work
$-6(34)7s(6)$ at 170 kHz	557.88	557.80	0.08	0.03	Magnetic field modulation	This work
$-6(34)7s(6)$ at 100 kHz	558.44	558.36	0.08	0.03	Magnetic field modulation	This work
Zero crossing near 556 G	556.26	556.19	0.07	0.03	Collapse of BEC	[80]
$-3(33)6g(3)$ at 368 kHz	553.44	553.44	−0.00	0.01	Magnetic field modulation	This work
Loss minimum (g) near 554 G	553.73	553.75	−0.02	0.01	Trap loss spectroscopy	This work
Loss maximum (g) near 554 G	554.06	554.07	−0.01	0.02	Trap loss spectroscopy	This work
Δ (g) near 554 G	0.33	0.32	0.01	0.01	Trap loss spectroscopy	This work
$-6(34)6s(6)$ at 1.7 MHz	890.52	890.61	−0.09	0.02	Magnetic field modulation	This work
$-6(34)6s(6)$ at 356 kHz	899.93	900.19	−0.26	0.03	Magnetic field modulation	This work
$-6(34)6s(6)$ at 110 kHz	915.66	915.54	0.12	0.03	Magnetic field modulation	This work
Zero crossing near 881 G	880.90	880.66	0.24	0.03	Collapse of BEC	[80]
$-6(34)6d(6)$ at 342 kHz	819.17	819.20	−0.03	0.03	Magnetic field modulation	This work
Loss minimum (d) near 820 G	819.41	819.37	0.04	0.03	Trap loss spectroscopy	This work
Loss maximum (d) near 820 G	820.37	820.33	0.04	0.02	Trap loss spectroscopy	This work
Δ (d) near 820 G	0.96	0.97	−0.01	0.05	Trap loss spectroscopy	This work

automated approach to fitting is unreliable: Individual least-squares steps often reach points in parameter space where the levels have moved too far to be identified reliably, particularly in the early stages of fitting. We therefore carried out the fitting using the I-NOLLS package [82] (interactive nonlinear least-squares), which gives the user interactive control over step lengths and assignments as the fit proceeds. This allowed us to converge on a minimum in the sum of weighted squares, with the parameters given in Table III.

The parameter uncertainties are given in Table III as 95% confidence limits [83]. However, it should be emphasized that these are *statistical* uncertainties within the particular parameter set. They do not include any errors due to the choice of the potential functions. Such model errors are far harder to estimate, except by performing a large number of fits with different potential models, which is not possible in the present case.

TABLE III. Parameters of the fitted potential.

	Fitted value	Confidence limit (95%)	Sensitivity
C_6 ($E_h a_0^6$)	6890.4768	0.081	0.0003
C_8 ($E_h a_0^8$)	1 009 289.6	2900	0.1
S_0 ($E_h a_0^{-2}$)	$3.172\,749 \times 10^{-4}$	2.5×10^{-6}	2.7×10^{-10}
S_1 ($E_h a_0^{-2}$)	$1.343\,217 \times 10^{-4}$	2.5×10^{-6}	1.3×10^{-10}
S_{2SO}	1.364 32	0.022	0.000 65
ρ_{ex}	0.978 845	0.0026	5.5×10^{-7}

In a correlated fit, the statistical uncertainty in a fitted parameter depends on the degree of correlation. However, to reproduce the results from a set of parameters, it is often necessary to specify many more digits than implied by the uncertainty. A guide to the number of digits required is given by the *parameter sensitivity* [83], which essentially measures how fast the observables change when one parameter is varied with all others held fixed. This quantity is included in Table III.

The singlet and triplet scattering lengths and the pole positions of the s-wave resonances are not directly observed quantities. Nevertheless, their values may be extracted from the final potential. In addition, the statistical uncertainties in derived parameters such as these may be obtained as described in Ref. [83]. The values and 95% uncertainties obtained in this way are given in Table IV.

A. Region between 800 and 920 G

In the region between 800 and 920 G, the near-threshold molecular structure and the corresponding scattering

TABLE IV. Comparison between key quantities calculated from different potentials.

Derived parameters	M2012	M2004
a_S (bohr)	286.5(1)	280.37(6)
a_T (bohr)	2858(19)	2440(24)
s pole near -10 (G)	$-12.38(8)$	
s pole near 550 (G)	548.78(9)	
s pole near 800 (G)	786.8(6)	

properties are relatively straightforward. As seen in Fig. 2, the ramping $-6(34)6s(6)$ state has a strong avoided crossing with $-2(33)6s(6)$ near 850 G at a binding energy of about 110 MHz. This crossing is still incomplete when the mixed state crosses the least-bound state $-1(33)6s(6)$ around 100 kHz. It is the state resulting from this second crossing that is observed at binding energies of 0.1 to 1.7 MHz between 890 and 920 G. These points are very well reproduced by the fit, as seen in Fig. 11. The $-3(34)6d(6)$ state that crosses the axis at 820.37 G is also well reproduced by the fit, as seen in Fig. 12.

The position of the s-wave resonance pole in this region has not been observed because of large three-body losses, but it is predicted by the fitted potential at 786.8(6) G. It is interesting to note that, because of the shift produced by the crossing with the least-bound state, the s-wave resonance occurs at a *lower* field than the corresponding d-wave resonance in this case, even though (as always) the unperturbed ramping s-wave state is lower in energy.

B. Region around 550 G

The region around 550 G is considerably more complicated. In this case the crossing between the ramping $-6(34)7s(6)$ state and $-2(33)6s(6)$ near 510 G is much narrower and so is almost complete by the time $-6(34)7s(6)$ crosses the least-bound state $-1(33)6s(6)$. This produces a zero crossing

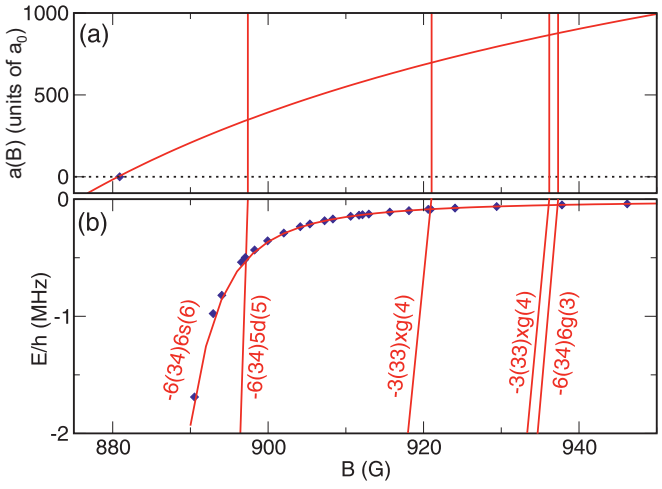

FIG. 11. (Color online) (a) The scattering length in the region between 875 and 950 G. The solid lines show results calculated for the M2012 potential with an sdg basis set. The diamond near 880 G indicates the position of the zero crossing. (b) The calculated bound-state energies with the same basis set. The diamonds show the measured energies in this region.

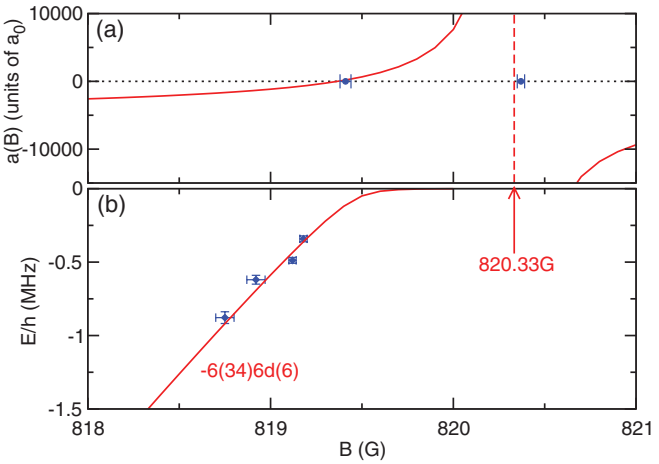

FIG. 12. (Color online) The scattering length and bound-state energy in the pole region of the $-6(34)6d(6)$ resonance. The solid lines show results from model M2012, calculated with an sdg basis set. The points in panel (a) show the measured pole position and loss minimum. The points in panel (b) show the measured binding energies. The dashed line in (a) and the arrow in (b) show the calculated pole position. Error bars refer to 1σ uncertainties.

near 556 G. However, as described in the experimental section, there is also a ramping $-3(33)3g(3)$ state that crosses threshold just below this, producing an additional pole and zero crossing near 554 G. Because of the large background scattering length arising from its proximity to the s-wave resonance, the g-wave resonance is far wider than is usual.

The bound-state measurements near 557 G are further complicated by an additional state that crosses and appears to mix with the s-wave state in the top 1 MHz. This cannot be assigned as s-, d-, or g-wave; it must be due to an i-wave state, and indeed the M2004 model predicts four i-wave levels to be in the range between around 530 and 590 G, with two between 555 and 565 G. However, these states are associated with hyperfine-excited thresholds, and their exact positions are very sensitive to details of the potential that do not significantly affect the other experimentally measured quantities considered here. We have been unable to decide unambiguously which one is responsible for the observed crossing. In addition, the i-wave states have very little influence on the s-wave scattering length that is the main object of interest in this region. We therefore decided to fit using a basis set with $L_{\max} = 4$, which excludes the i-wave states entirely, and also to exclude from the fit any binding energies affected by the crossing between the s- and i-wave states.

The general fit to the ramping s-wave bound state is shown in Fig. 13 and an expanded view of the fir to the g-wave state is shown in Fig. 14. It may be seen that the calculated s-wave state passes well through the experimental points either side of the crossing with the i-wave state, while the calculated g-wave state reproduces the bound-state energies as well as the zero crossing and pole in the scattering length.

The crossing between the i-wave state and the $-6(34)7s(6)$ state near 557 G is surprisingly strongly avoided. As described above, we were unable to ramp the magnetic field fast enough to transfer a detectable number of molecules between the two states, which sets a lower limit of 30 kHz to the strength of

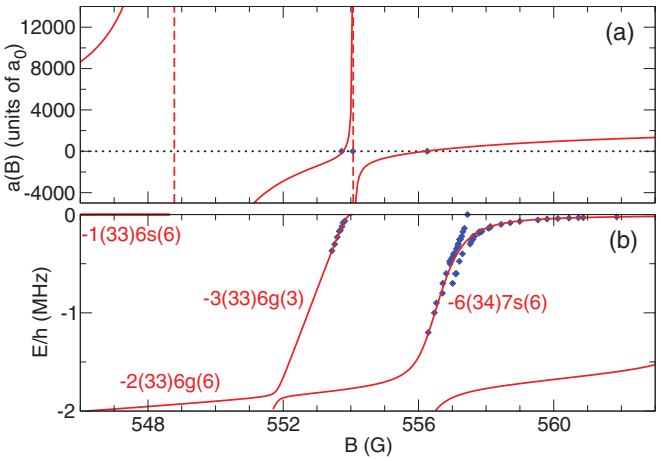

FIG. 13. (Color online) (a) The scattering length between 546 and 564 G. The solid lines show results calculated for the M2012 potential with an *sdg* basis set. The diamonds show the measured pole position and loss minimum near 554 G and the zero crossing near 556 G. The dashed line shows the calculated pole position. (b) The calculated binding energies with the same basis set as for panel (a). The diamonds show the measured binding energies.

the avoided crossing. In a zeroth-order picture, the two states are separated by $\Delta L = 6$ and the only coupling off-diagonal in L is $\hat{V}^{\rm d}(R)$, which can couple only $\Delta L = 2$ and is quite small. However, quantitative modeling of this effect requires a theoretical model that places the i-wave state in the correct place. This is likely to require simultaneous modeling of the present results and the spectroscopy of more deeply bound levels, and this remains a subject for future work.

C. Low-field region

The low-field region, below 60 G, is also quite complicated. The ramping s-wave state responsible for the Efimov resonances in this region is $-7(44)6s(6)$. However, there are

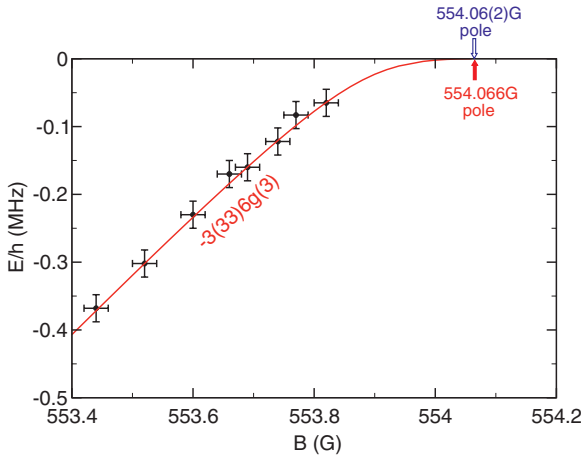

FIG. 14. (Color online) Expanded view of the scattering length in the pole region of the $-3(33)6g(3)$ resonance. The solid line shows results calculated for the M2012 potential with an *sdg* basis set. The points show the measured bound-state energies. The calculated and measured pole positions are indicated by solid and open arrows, respectively. Error bars refer to 1σ uncertainties.

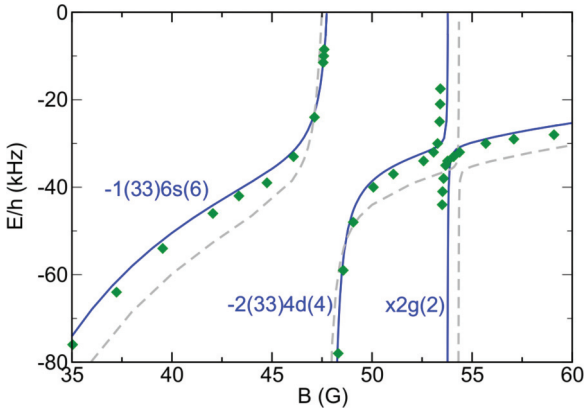

FIG. 15. (Color online) The bound-state energies between 35 and 60 G. The solid lines show results calculated for the M2012 potential with an *sdg* basis set, showing one side of the avoided crossings of the $-7(44)6s(6)$ bound state with the $-1(33)6s(6)$ least-bound state in the threshold entrance channel. The points show the previously measured bound-state energies [14,37]. The agreement is much better with the new M2012 model than with the old M2004 model, shown as light dashed lines.

also families of ramping $-2(33)6g$ states that cross threshold between 4 and 8 G and $-2(33)4g$ states that cross between 11 and 21 G. In addition, there is a $-2(33)4d(4)$ state that crosses near 48 G and a $2g(2)$ state that crosses near 54 G. The latter state does not carry a clear $n(f_1 f_2)$ signature, but it clearly has $2g(2)$ character.

The binding energies of many of these states have been measured by magnetic moment spectroscopy at binding energies up to about 10 MHz [14], though these measurements have significant uncertainties associated with the integration over field. However, there are much more precise results for the $-7(44)6s(6)$ state as it crosses with the least-bound state, obtained from microwave spectroscopy [14] and magnetic field modulation spectroscopy [37]. Particularly important are measurements of the crossing between this mixed state and the $-2(33)4d(4)$ state near 48 G, since the strength of this crossing provides the most direct experimental information available on the strength of the second-order spin-orbit coupling and thus on the potential parameter $S_{\rm 2SO}$.

Figures 15 and 16 show the overall fit to the bound states below 60 G for both the M2004 and the M2012 potentials. The ramping s-wave state between 17 and 60 G is of particular interest. This state switches from $-7(44)6s(6)$ to $-1(33)6s(6)$ character as B increases. All the experimental energies are well reproduced, including those near the two avoided crossings with the $4d(4)$ and $2g(2)$ states shown in Fig. 15. Even in this region, the M2012 model agrees with the experimental results significantly better than the M2004 model.

D. Independent tests of the M2012 model

The older potential models [9,10] satisfactorily reproduced the bound states for s-, d-, and g-wave states at fields below 60 G. However, the measurements also revealed the existence of l-wave ($L = 8$) states [14,15], which do not lead to observable Feshbach resonances because of their very weak coupling to the s-wave threshold channel. The M2004 model failed for

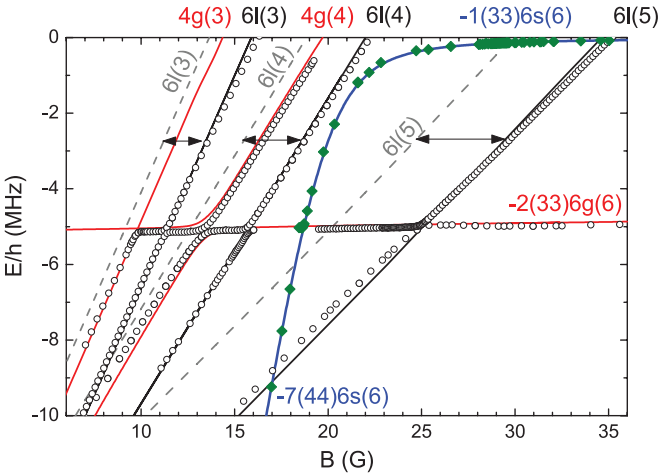

FIG. 16. (Color online) Comparison between experimental results for s-wave levels (diamonds [14,37]) and g- and l-wave levels (open circles [14,15]) with the results of the M2012 model (solid lines). Only levels for which experimental results exist are shown. The s-wave and g-wave levels are calculated with the full sdg basis set. The l-wave levels are calculated with an l basis only. The light dashed lines show the l-wave levels calculated with the M2004 model. The arrows show the separation between equivalent levels in the M2004 and M2012 models. The additional quantum numbers $n(f_1 f_2)$ are $-2(33)$ for the two $4g$ levels and $-3(33)$ for the three $6l$ levels.

these l-wave states, with errors of up to 5 G in the positions at a given bound-state energy. The l-wave states were not included explicitly in our fits, but the comparison between the calculated levels and experiment is shown in Fig. 16 for both the current model M2012 and the older M2004 one. It is clear that M2012 gives a far more satisfactory reproduction of the experimental l-wave levels.

There is a particularly interesting region near 500 G, where a group of four strongly coupled $-6(34)7d(M_F)$ levels cross threshold. The underlying levels have M_F values of 4, 5, 6, and 7, but are strongly mixed with one another so that M_F is not a good quantum number for the actual eigenstates. The bound states have not yet been measured in this region, but the calculated levels are shown in Fig. 17, together with the calculated scattering length and the positions of the measured loss maxima and minima. The loss maxima are well reproduced. The two loss minima at 499.6 and 502.15 G are also well reproduced by the model, but the loss minimum at 492.8 G is not near a zero-crossing of the calculated scattering length. However, there are two strong overlapping and interfering resonances with poles in $a(B)$ at 492.7 and 495.0 G, and it is not clear how to interpret the three-body loss in such a region. This complex region from 490 to 510 G needs further investigation, especially since it may display rich Efimov physics [52].

E. Mapping between scattering length and magnetic field

An important goal of this paper is to develop a theoretical model that is capable of giving an accurate mapping between the scattering length $a(B)$ and the magnetic field B, with particular focus on collisions between two Cs atoms in the lowest Zeeman level of the ground-state manifold. Our new

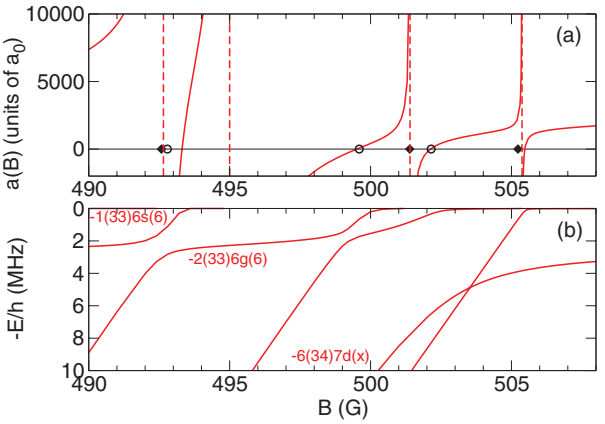

FIG. 17. (Color online) The scattering length (a) and bound-state energies (b) between 490 and 508 G, calculated for the M2012 potential with an sdg basis set. The solid diamonds in (a) show the positions of experimental loss maxima and the open circles show the positions of loss minima. The four ramping $-6(34)7d(x)$ levels, labeled collectively by x since their M_F components are mixed, undergo avoided crossings with the $-2(33)6g(6)$ level that passes through this region with $-E/h \approx 2$ MHz. The avoided crossings with the least-bound level $-1(33)6s(6)$ near $-E/h \approx 0.01$ MHz are too close to the $E = 0$ line to be seen on the figure.

M2012 model is based on realistic potentials and includes the full spin Hamiltonian for the Cs_2 molecule at long range. It has been calibrated against experimental binding energies and a large number of resonance positions at magnetic fields between 0 and 1000 G. We therefore expect it to provide an accurate representation of $a(B)$ across this entire range of fields. Figure 18 shows $a(B)$ on a grid with 0.1 G spacing over the new experimental range between 460 and 1000 G. At this resolution, some narrow resonances are not fully resolved, and the narrowest ones are not visible at all.

The Supplemental Material [29] provides a tabulation of $a(B)$ against B over the full range of fields from 0 to 1200 G,

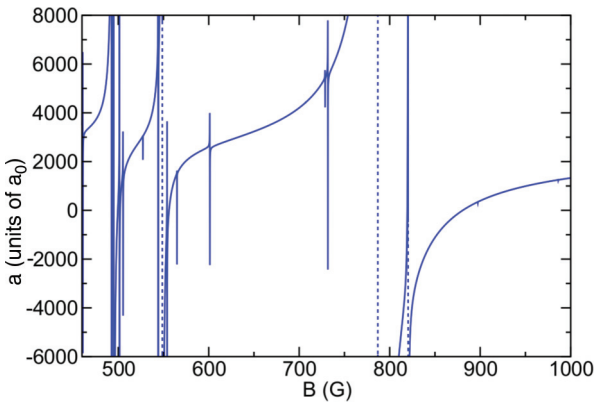

FIG. 18. (Color online) The scattering length between 460 and 1000 G, calculated for the M2012 potential with an sdg basis set. The dashed lines indicate the pole positions of the broad s-wave resonances near 549 and 787 G and the d-wave one near 820 G. Note that some narrow resonances appear as spikes because of the limited grid spacing of 0.1 G, and some of the narrowest are not visible at all.

for use in interpreting experiments. Additional tables lists all s-, d-, g-, i-, and l-wave resonances up to 1000 G.

VI. CONCLUSION

We have explored the scattering properties of ground-state Cs atoms and the binding energies of weakly bound Cs_2 molecules in the previously uncharted magnetic field range up to 1000 G, using a combination of experiment and theory. We have developed a model of the interaction potential that reproduces the experiments accurately over the entire range of magnetic fields studied.

Experimentally, we have investigated Feshbach resonances and dimer binding energies in the magnetic field range between 450 and 1000 G, utilizing an ultracold Cs sample in an optical dipole trap. Around 550 and 800 G, we verified that the general scattering properties of atomic Cs are governed by two broad s-wave Feshbach resonances. Fifteen Feshbach resonances stemming from molecular states with $L > 0$ were pinpointed by trap loss spectroscopy. We found evidence for the existence of i-wave Feshbach resonances, resulting from the coupling of molecular states with $L = 6$ to the atomic threshold. By performing magnetic field modulation spectroscopy, we determined the binding energies of several dimer states, paying particular attention to the two s-wave states that are responsible for the general Cs scattering properties in the high-field region.

To calculate the scattering properties and bound-state energies, we solve the Schrödinger equation using coupled-channel methods. We carried out direct least-squares fitting to the combined experimental data of this article and Refs. [14,32,37,38,80] to obtain a six-parameter model of the long-range interaction potential, which we designate M2012.

The M2012 potential reproduces the experimental results much better than the earlier M2004 potential [9], particularly at higher fields (above 250 G). It also predicts i-wave and l-wave states, which were not included in the least-squares fits. The calculated positions of l-wave bound states agree well with the experimental results reported in Ref. [15], for which the M2004 potential failed; this demonstrates the predictive power of the model. The pole positions of the two broad s-wave Feshbach resonances at high field are calculated to be 548.78 and 786.80 G for the $-6(34)7s(6)$ and the $-6(34)6s(6)$ states, respectively.

The M2012 potential does have some remaining deficiencies. In particular, it is fitted only to results from ultracold collisions and the bound states that lies within 10 MHz of the atomic threshold. It does not include results from electronic spectroscopy on deeply bound levels of Cs_2, or the near-dissociation levels observed in two-color photoassociation spectroscopy [84], which are bound by 5 to 80 GHz. It also does not satisfactorily reproduce the positions of i-wave states associated with excited hyperfine thresholds. Resolving these remaining issues will require a simultaneous fit to all the experiments together and is a topic for future work.

Our model allows us to make an accurate connection between the experimentally controllable magnetic field strength B and the s-wave scattering length a over a wide range of fields. The scattering length is the essential parameter in universal theories, and this connection was crucial in allowing us to interpret our measurements of three-body recombination in terms of universal Efimov physics in Ref. [18]. The present work is important not only for experiments on Cs, but also provides important information for ongoing and future experiments involving Cs mixtures, such as RbCs [85], LiCs [86,87], and other interesting combinations.

ACKNOWLEDGMENTS

We acknowledge support by the Austrian Science Fund FWF within Project No. P23106. A.Z. was supported within the Marie Curie Intra-European Program of the European Commission (Project No. LatTriCs). P.S.J. and J.M.H. acknowledge support from EPSRC, AFOSR MURI Grant No. FA9550-09-1-0617, and EOARD Grant No. FA8655-10-1-3033.

[1] C. Chin, R. Grimm, P. S. Julienne, and E. Tiesinga, Rev. Mod. Phys. **82**, 1225 (2010).
[2] J. Herbig, T. Kraemer, M. Mark, T. Weber, C. Chin, H.-C. Nägerl, and R. Grimm, Science **301**, 1510 (2003).
[3] J. G. Danzl, E. Haller, M. Gustavsson, M. J. Mark, R. Hart, N. Bouloufa, O. Dulieu, H. Ritsch, and H.-C. Nägerl, Science **321**, 1062 (2008).
[4] J. G. Danzl, M. J. Mark, E. Haller, M. Gustavsson, R. Hart, J. Aldegunde, J. M. Hutson, and H.-C. Nägerl, Nat. Phys. **6**, 265 (2010).
[5] Units of gauss rather than tesla, the accepted SI unit for the magnetic field, have been used in this paper to conform to the conventional usage in this field of physics.
[6] V. Vuletić, A. J. Kerman, C. Chin, and S. Chu, Phys. Rev. Lett. **82**, 1406 (1999).
[7] C. Chin, V. Vuletić, A. J. Kerman, and S. Chu, Phys. Rev. Lett. **85**, 2717 (2000).
[8] C. Chin, A. J. Kerman, V. Vuletić, and S. Chu, Phys. Rev. Lett. **90**, 033201 (2003).
[9] C. Chin, V. Vuletić, A. J. Kerman, S. Chu, E. Tiesinga, P. J. Leo, and C. J. Williams, Phys. Rev. A **70**, 032701 (2004).
[10] P. J. Leo, C. J. Williams, and P. S. Julienne, Phys. Rev. Lett. **85**, 2721 (2000).
[11] P. J. Leo, P. S. Julienne, F. H. Mies, and C. J. Williams, Phys. Rev. Lett. **86**, 3743 (2001).
[12] J. Söding, D. Guéry-Odelin, P. Desbiolles, G. Ferrari, and J. Dalibard, Phys. Rev. Lett. **80**, 1869 (1998).
[13] T. Weber, J. Herbig, M. Mark, H.-C. Nägerl, and R. Grimm, Science **299**, 232 (2003).
[14] M. Mark, F. Ferlaino, S. Knoop, J. G. Danzl, T. Kraemer, C. Chin, H.-C. Nägerl, and R. Grimm, Phys. Rev. A **76**, 042514 (2007).
[15] S. Knoop, M. Mark, F. Ferlaino, J. G. Danzl, T. Kraemer, H.-C. Nägerl, and R. Grimm, Phys. Rev. Lett. **100**, 083002 (2008).

[16] V. Efimov, Phys. Lett. B **33**, 563 (1970).
[17] T. Kraemer, M. Mark, P. Waldburger, J. G. Danzl, C. Chin, B. Engeser, A. D. Lange, K. Pilch, A. Jaakkola, H.-C. Nägerl, and R. Grimm, Nature (London) **440**, 315 (2006).
[18] M. Berninger, A. Zenesini, B. Huang, W. Harm, H.-C. Nägerl, F. Ferlaino, R. Grimm, P. S. Julienne, and J. M. Hutson, Phys. Rev. Lett. **107**, 120401 (2011).
[19] J. P. D'Incao, C. H. Greene, and B. D. Esry, J. Phys. B **42**, 044016 (2009).
[20] J. Wang, J. P. D'Incao, B. D. Esry, and C. H. Greene, Phys. Rev. Lett. **108**, 263001 (2012).
[21] P. Naidon, S. Endo, and M. Ueda, arXiv:1208.3912.
[22] R. Schmidt, S. P. Rath, and W. Zwerger, Eur. Phys. J. B **85**, 386 (2012).
[23] C. Chin, arXiv:1111.1484.
[24] S. E. Pollack, D. Dries, and R. G. Hulet, Science **326**, 1683 (2009).
[25] N. Gross, Z. Shotan, S. Kokkelmans, and L. Khaykovich, Phys. Rev. Lett. **103**, 163202 (2009).
[26] T. B. Ottenstein, T. Lompe, M. Kohnen, A. N. Wenz, and S. Jochim, Phys. Rev. Lett. **101**, 203202 (2008).
[27] J. H. Huckans, J. R. Williams, E. L. Hazlett, R. W. Stites, and K. M. O'Hara, Phys. Rev. Lett. **102**, 165302 (2009).
[28] R. J. Wild, P. Makotyn, J. M. Pino, E. A. Cornell, and D. S. Jin, Phys. Rev. Lett. **108**, 145305 (2012).
[29] See Supplemental Material at http://link.aps.org/supplemental/10.1103/PhysRevA.87.032517 for a tabulation of $a(B)$ against B from 0 to 1200 G and tables listing all s-, d-, g-, i-, and l-wave Feshbach resonances up to 1000 G.
[30] P. S. Julienne, E. Tiesinga, and T. Köhler, J. Mod. Opt. **51**, 1787 (2004).
[31] P. S. Julienne and B. Gao, in *Atomic Physics 20*, edited by C. Roos, H. Häffner, and R. Blatt, AIP Conf. Proc. No. 869 (AIP, New York, 2006), pp. 261–268.
[32] J. M. Hutson, E. Tiesinga, and P. S. Julienne, Phys. Rev. A **78**, 052703 (2008). Note that the matrix element of the dipolar spin-spin operator given in Eq. (A2) of this paper omits a factor of $-\sqrt{30}$.
[33] D. Guéry-Odelin, J. Söding, P. Desbiolles, and J. Dalibard, Europhys. Lett. **44**, 25 (1998).
[34] D. Guéry-Odelin, J. Söding, P. Desbiolles, and J. Dalibard, Opt. Exp. **2**, 323 (1998).
[35] S. A. Hopkins, S. Webster, J. Arlt, P. Bance, S. Cornish, O. Maragò, and C. J. Foot, Phys. Rev. A **61**, 032707 (2000).
[36] J. Arlt, P. Bance, S. Hopkins, J. Martin, S. Webster, A. Wilson, K. Zetie, and C. J. Foot, J. Phys. B **31**, L321 (1998).
[37] A. D. Lange, K. Pilch, A. Prantner, F. Ferlaino, B. Engeser, H.-C. Nägerl, R. Grimm, and C. Chin, Phys. Rev. A **79**, 013622 (2009).
[38] M. Gustavsson, E. Haller, M. J. Mark, J. G. Danzl, G. Rojas-Kopeinig, and H.-C. Nägerl, Phys. Rev. Lett. **100**, 080404 (2008).
[39] M. Gustavsson, Ph.D. thesis, University of Innsbruck, 2008.
[40] M. Berninger, Ph.D. thesis, University of Innsbruck, 2011.
[41] T. Kraemer, J. Herbig, M. Mark, T. Weber, C. Chin, H.-C. Nägerl, and R. Grimm, Appl. Phys. B **79**, 1013 (2004).
[42] T. Weber, Ph.D. thesis, University of Innsbruck, 2003.
[43] A. J. Kerman, V. Vuletić, C. Chin, and S. Chu, Phys. Rev. Lett. **84**, 439 (2000).
[44] P. Treutlein, K. Y. Chung, and S. Chu, Phys. Rev. A **63**, 051401(R) (2001).
[45] R. Grimm, M. Weidemüller, and Y. B. Ovchinnikov, Adv. At. Mol. Opt. Phys. **42**, 95 (2000).
[46] T. Weber, J. Herbig, M. Mark, H.-C. Nägerl, and R. Grimm, Phys. Rev. Lett. **91**, 123201 (2003).
[47] G. Breit and I. I. Rabi, Phys. Rev. **38**, 2082 (1931).
[48] J. P. D'Incao, H. Suno, and B. D. Esry, Phys. Rev. Lett. **93**, 123201 (2004).
[49] P. O. Fedichev, M. W. Reynolds, and G. V. Shlyapnikov, Phys. Rev. Lett. **77**, 2921 (1996).
[50] B. D. Esry, C. H. Greene, and J. P. Burke, Phys. Rev. Lett. **83**, 1751 (1999).
[51] E. Nielsen and J. H. Macek, Phys. Rev. Lett. **83**, 1566 (1999).
[52] F. Ferlaino, A. Zenesini, M. Berninger, B. Huang, H.-C. Nägerl, and R. Grimm, Few-Body Syst. **51**, 113 (2011).
[53] S. T. Thompson, E. Hodby, and C. E. Wieman, Phys. Rev. Lett. **95**, 190404 (2005).
[54] C. Weber, G. Barontini, J. Catani, G. Thalhammer, M. Inguscio, and F. Minardi, Phys. Rev. A **78**, 061601(R) (2008).
[55] G. Thalhammer, G. Barontini, J. Catani, F. Rabatti, C. Weber, A. Simoni, F. Minardi, and M. Inguscio, New J. Phys. **11**, 055044 (2009).
[56] Q. Beaufils, A. Crubellier, T. Zanon, B. Laburthe-Tolra, É. Maréchal, L. Vernac, and O. Gorceix, Eur. Phys. J. D **56**, 99 (2010).
[57] B. Pasquiou, G. Bismut, Q. Beaufils, A. Crubellier, E. Maréchal, P. Pedri, L. Vernac, O. Gorceix, and B. Laburthe-Tolra, Phys. Rev. A **81**, 042716 (2010).
[58] N. Gross, Z. Shotan, S. Kokkelmans, and L. Khaykovich, Phys. Rev. Lett. **105**, 103203 (2010).
[59] R. Napolitano, J. Weiner, C. J. Williams, and P. S. Julienne, Phys. Rev. Lett. **73**, 1352 (1994).
[60] L. Landau, Phys. Z. Sowjetunion **2**, 46 (1932).
[61] C. Zener, Proc. R. Soc. London A **137**, 696 (1932).
[62] J. M. Hutson and S. Green, MOLSCAT *computer program, version 14*, distributed by Collaborative Computational Project No. 6 (UK Engineering and Physical Sciences Research Council, Swindon, UK, 1994).
[63] M. L. González-Martínez and J. M. Hutson, Phys. Rev. A **75**, 022702 (2007).
[64] D. E. Manolopoulos, J. Chem. Phys. **85**, 6425 (1986).
[65] M. H. Alexander and D. E. Manolopoulos, J. Comput. Phys. **86**, 2044 (1987).
[66] M. H. Alexander, J. Chem. Phys. **81**, 4510 (1984).
[67] B. R. Johnson, J. Comput. Phys. **13**, 445 (1973).
[68] J. M. Hutson, New J. Phys. **9**, 152 (2007).
[69] J. M. Hutson, BOUND computer program, version 5, distributed by Collaborative Computational Project No. 6 (UK Engineering and Physical Sciences Research Council, Swindon, UK, 1993).
[70] J. M. Hutson, Comput. Phys. Commun. **84**, 1 (1994).
[71] J. M. Hutson, FIELD computer program, version 1 (2011).
[72] M. Marinescu, J. F. Babb, and A. Dalgarno, Phys. Rev. A **50**, 3096 (1994).
[73] B. M. Smirnov and M. I. Chibisov, Sov. Phys. JETP **21**, 624 (1965).
[74] M. Krauss and W. J. Stevens, J. Chem. Phys. **93**, 4236 (1990).
[75] H. Akima, ACM Trans. Math. Softw. **17**, 341 (1991).
[76] H. T. C. Stoof, J. M. V. A. Koelman, and B. J. Verhaar, Phys. Rev. B **38**, 4688 (1988).

[77] A. J. Moerdijk, B. J. Verhaar, and A. Axelsson, Phys. Rev. A **51**, 4852 (1995).
[78] F. H. Mies, C. J. Williams, P. S. Julienne, and M. Krauss, J. Res. Natl. Inst. Stand. Technol **101**, 521 (1996).
[79] S. Kotochigova, E. Tiesinga, and P. S. Julienne, Phys. Rev. A **63**, 012517 (2000).
[80] A. Zenesini, B. Huang, M. Berninger, S. Besler, H.-C. Nägerl, F. Ferlaino, and R. Grimm (unpublished).
[81] In order to obtain a good fit to the experimental results in the regions important for Efimov physics, the uncertainties used here differ from the experimental uncertainties in some cases.
[82] M. M. Law and J. M. Hutson, Comput. Phys. Commun. **102**, 252 (1997).
[83] R. J. Le Roy, J. Mol. Spectrosc. **191**, 223 (1998).
[84] N. Vanhaecke, C. Lisdat, B. T'Jampens, D. Comparat, A. Crubellier, and P. Pillet, Eur. Phys. J. D **28**, 351 (2004).
[85] T. Takekoshi, M. Debatin, R. Rameshan, F. Ferlaino, R. Grimm, H.-C. Nägerl, C. R. Le Sueur, J. M. Hutson, P. S. Julienne, S. Kotochigova, and E. Tiemann, Phys. Rev. A **85**, 032506 (2012).
[86] M. Repp, R. Pires, J. Ulmanis, R. Heck, E. D. Kuhnle, M. Weidemüller, and E. Tiemann, Phys. Rev. A **87**, 010701(R) (2013).
[87] S.-K. Tung, C. Parker, J. Johansen, C. Chin, Y. Wang, and P. S. Julienne, Phys. Rev. A **87**, 010702(R) (2013).